Radio Frequency Based Vascular Dementia Sensing and Imaging System Targeting Smart Glasses

Radio Frequency Based Vascular Dementia Sensing and Imaging System Targeting Smart Glasses

Usman Anwar, *Graduate Student Member, IEEE*, Tughrul Arslan, *Senior Member, IEEE*, Peter Lomax and Tom C. Russ

***Abstract*— Vascular dementia is the second most prevalent type of dementia among the elderly population and is one of the leading causes of mortality. Ischemic stroke and brain atrophy are the predominant pathologies associated with vascular dementia. Early detection and regular monitoring are crucial to prevent the advancement of vascular dementia. Conventional medical imaging is expensive, requires extensive medical supervision and is not easily accessible. This research presents a novel concept of low-cost and non-invasive smart glasses, equipped with miniaturized octagonal monopole-patch antenna (OMPA) sensors and a crescent array sensor for vascular dementia detection. This Radio Frequency (RF) enabled portable system is capable of accurately identifying and imaging brain infarction, atrophy and stroke in their early stages. The fabricated device is experimentally verified using multiple artificial stroke and atrophy targets inside a realistic brain phantom. The backscattered RF data is iteratively processed using customized imaging algorithms to achieve improved image quality, noise suppression, and contrast resolution with reduced image artifacts and computational complexity. Based on the iterative refinement, the Double Stage Minimum Variance Delay Multiply and Sum (DS-MV-DMAS) algorithm is proposed for imaging stroke and brain atrophy. The quantitative results indicate that DS-MV-DMAS results in 43% lower level of side lobes and leads to 26%, 28% and 27% improvement in signal-to-noise ratio, full width at half-maximum and contrast ratio, respectively, compared to other state-of-the-art imaging algorithms. The promising results demonstrate the feasibility of the prototype system as a cost-effective, portable and non-invasive alternative for the diagnosis and monitoring of vascular dementia.**

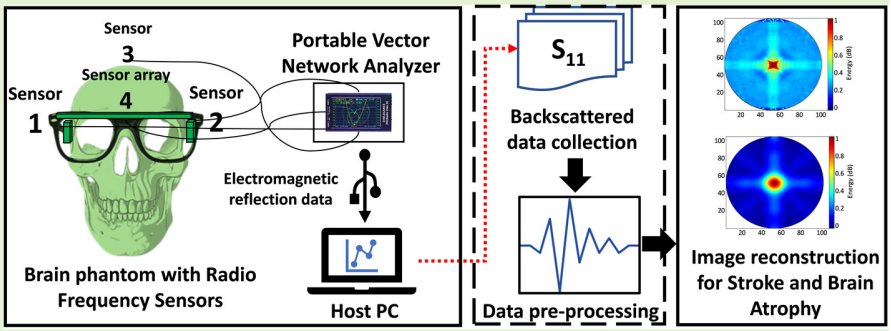

***Index Terms*— Brain atrophy, Microwave Medical Imaging, Non-invasive sensors, Radio Frequency sensing, Stroke, Vascular Dementia**

I. Introduction

VASCULAR dementia is considered to be the second most common form of dementia after Alzheimer's disease. Around 17 percent of people above 65 years of age with dementia have vascular dementia [1]. Vascular dementia typically starts with a decreased blood flow to the brain due to blood clots or vascular blockage in various segments of the brain [2]. This results in vascular impairment, infarcts, white matter lesions and brain atrophy in some cases. Other underlying factors that lead to vascular dementia include high blood pressure, hyperlipidemia, diabetes, cardiovascular disease, stroke and hearing loss [3]. Initial pathological changes occur in the white matter of the brain that are followed by micro and macro-infarcts. In some cases, this leads to brain atrophy due to cerebrovascular impairment and long-term reduced blood flow in the brain [4]. The damage caused by the infarction is mostly irreversible; however, a timely diagnosis can help avoid future cerebrovascular incidents. Due to the progressive nature of vascular dementia, regular monitoring is critical for timely diagnosis and disease management. Brain imaging is an essential tool for diagnosis and determines future treatment options available to the patient. Currently, Magnetic Resonance Imaging (MRI), Positron Emission Tomography (PET) [5], carotid ultrasound [6] and Computerized Tomography (CT)

This paper was submitted on July 17, 2024. This work was supported in part by U.K. Engineering and Physical Sciences Research Council (EPSRC) under Grant EP/T021063/1; and in part by the Higher Education Commission (HEC), Pakistan.

U. Anwar, T. Arslan and P. Lomax are with the School of Engineering, The University of Edinburgh, Edinburgh, United Kingdom (Email: Usman.Anwar@ed.ac.uk, Tughrul.Arslan@ed.ac.uk, Peter.Lomax@ed.ac.uk).

Tom C. Russ is Director of the Alzheimer Scotland Dementia Research Centre at The University of Edinburgh, United Kingdom (Email: T.C.Russ@ed.ac.uk)

.

scans [7] are primarily used for brain imaging and vascular dementia diagnosis. These conventional imaging systems require medical expertise, and supervision in addition to high operational and maintenance costs. The timely availability of diagnostic systems to patients is critical in the case of ischemic stroke.

Radio Frequency (RF) and microwave technologies provide effective sensing and diagnosis through compact, low-cost, non-invasive, non-ionizing and wearable sensors. Microwave frequencies in the Ultra-wideband (UWB) range are primarily being used for diagnostic applications. Microwave sensors have been reported in recent studies for monitoring dehydration [8], blood glucose [9][10], blood biomarkers, and vital signs [11]. Microwave sensors were utilized for non-invasive, real-time blood glucose monitoring by detecting variations in the dielectric properties of blood-mimicking solutions [10]. Another study introduced a reconfigurable multimode microwave sensor that combines resonance and transmission sensing to achieve high-sensitivity glycemia detection [9]. This was achieved by analyzing shifts in multiple resonance frequencies and changes in the amplitude of the transmission coefficient within a specific operating band. RF signals can easily penetrate the skull to propagate through the biological tissues and layers within the brain [12]. The backscattered signals are collected back at the RF sensors to detect the physiological and pathophysiological degenerations. The reflection data received at the sensing device can be used for image reconstruction using integrated software algorithms.

Recent research in head diagnostics has shown significant improvement in terms of image resolution, device sensitivity and clinical feasibility. The existing research mostly focuses on inverse scattering imaging techniques, supported by computational algorithms to reconstruct high-resolution images. Microwave imaging was proposed for whole-brain atrophy detection using Microwave Imaging via Space-Time (MIST) [13]. The algorithm is validated on real lamb brain phantoms with different levels of atrophy. A frequency-based imaging technique with clutter removal is presented for microwave brain imaging [14]. An eight-element antenna array is used to collect the reflection data, and the average subtraction method is applied to mitigate the clutter effect in each frequency step. A portable microwave imaging system with eight elements tapered slot Vivaldi antenna array is presented for breast tumor detection [15]. The system is supported by the Iteratively Corrected Delay and Sum (IC-DAS) algorithm, which iteratively enhances the imaging of tumorous cells within a breast phantom. A microwave brain imaging system with an array of twenty-four monopole antennas is designed for stroke detection and imaging [16]. The system is capable of imaging both intracranial hemorrhagic and ischemic strokes with a truncated singular value decomposition (TSVD) based algorithm. An ultra-wideband horn antenna array with eight rotatable antennas is presented for haemorrhagic stroke detection [17]. Despite its effectiveness in identifying strokes and lesions, the system is non-portable and only supports static operation. A portable wideband microwave imaging system with a rotatable platform is presented for intracranial hemorrhage detection and imaging [18]. The system is validated on an MRI-based realistic head phantom. Although these techniques are effective in the detection of brain stroke, Alzheimer's and breast cancer, these imaging techniques operate with static multi-element antenna arrays for complete head coverage. This requires constant supervision to operate and may not be comfortable for ageing patients.

The proposed work extends our previous work on vascular dementia detection and imaging using the Microwave Imaging via Space-Time (MIST) algorithm [19]. A novel concept of smart RF glasses is presented for sensing and imaging stroke and brain atrophy, the hallmarks of vascular dementia. The proposed device is planned to integrate with the next-generation multimodal hearing aids, as part of the COG-MHEAR project [20]. Hearing loss is a major factor to contribute towards the rapid progression of dementia and brain atrophy [21]. Persistent hearing loss doubles the risk of developing dementia [22]. These multimodal hearing aids with smart RF glasses will provide a preemptive detection of early dementia onset. The proposed smart glasses are integrated with Ultra-wideband (UWB) antennas for brain sensing and imaging. UWB antennas generate and receive electromagnetic waves across a wide frequency range to capture physiological changes within the brain. The dielectric contrast between the healthy and diseased areas of the brain results in the creation of distinct microwave images, potentially aiding in the early detection of vascular dementia. This research presents novel, low-profile, non-ionizing and cost-effective RF glasses to detect the dielectric variations within the brain. A highly directive octagonal monopole-patch antenna (OMPA) sensor is designed to integrate with the side hinge of glasses to scan the temporal and parietal regions. A miniaturized crescent antenna array is installed on the front bridge of RF glasses to scan the frontal lobe, prefrontal cortex, and occipital lobe.

The microwave imaging techniques available in the literature can detect neurodegenerative pathologies, but these are specifically designed to detect single anomalies. The proposed glasses-based imaging system can reconstruct high-contrast stroke and brain atrophy images using a tailored microwave beamforming algorithm, and the non-invasive system is highly suitable for adaptable dementia care. The novel aspects and contributions of this research are:

- A novel, low-cost, non-invasive smart glasses with miniaturized RF sensors is presented for brain sensing and imaging. The proposed system can detect both stroke and brain atrophy, unlike existing imaging techniques that focus on single anomalies [15][17].
- Crescent array is designed to integrate with the glasses' bridge frame. The first-of-its-kind dual-element array provides high sensitivity and directivity to scan the frontal lobe and prefrontal cortex of the brain.
- The OMPA and crescent microstrip antennas offer high conformability, low profile, flexibility, high sensitivity, cost-effectiveness and ease of fabrication in contrast to horn and Vivaldi antennas reported in the literature [15] [17].
- The methodology opted for imaging requires fewer sensors for complete brain coverage as compared to the state-of-the-art techniques available in the literature [15][16].
- The proposed DS-MV-DMAS algorithm can reconstruct stroke and brain atrophy images with a 43% lower level of side lobes and leads to 26%, 28% and 27% improvement

in signal-to-noise ratio, full width at half-maximum and contrast ratio, respectively, compared to other state-of-the-art beamforming algorithms.

The rest of this paper is arranged as follows: methodology is discussed in Section II. The design and configuration of RF sensors are discussed in Section III. Section IV provides an analysis of near-field software simulations. The experimental results for validation of the proposed RF sensing and imaging system are discussed. The sensor measurements are processed using customized confocal imaging algorithms and a detailed comparison is presented. A customized imaging algorithm is proposed for two-dimensional brain imaging with stroke and atrophy targets. The paper concludes with a discussion on the future scope of this work in dementia research and clinical arrangements.

II. Context And Methodology

Stroke and brain atrophy associated with vascular dementia involve structural changes in the brain, which leads to dielectric alterations in the affected tissues. The clot formation also results in abnormal blood vessel formation, which usually leads to inflammation and edema. The disruption of blood flow to certain parts of the brain affects cell membrane permeability and ion concentrations within the affected area. These metabolic changes affect the concentration of protein and metabolites within the brain, which contributes to dielectric contrast. In severe brain stroke, cellular death leads to tissue necrosis, which can also impact the dielectric properties of the affected region. A brain atrophy leads to a reduction in cellular density, which impacts the dielectric properties of pathological tissue. The atrophy also affects the water content, blood flow and ventricular size within the brain. The ventricular changes impact the distribution of cerebrospinal fluid (CSF) within the brain. As the CSF is more conductive due to higher water content and lower cellular composition, the accumulation of CSF in the atrophy region contributes to the changes in the dielectric properties of pathological tissue. This paper presents a novel application of wearable, non-invasive, non-ionizing and low-cost RF glasses for the diagnosis of vascular dementia through the detection and investigation of major pathological changes in the brain.

In the first phase of research, antenna sensors were designed through simulations on CST Microwave Studio. The performance of optimized RF sensors is validated on software head voxel models to capture the pathophysiological degeneration within the brain. In the second phase, the miniaturized RF sensors were fabricated and integrated with glasses to monitor the progression of vascular dementia. The minimalistic design of RF glasses offers convenient operability. Experimental validation was performed on a heterogeneous brain phantom with dielectric properties similar to a real human brain. Stroke and brain atrophy targets were integrated within the realistic phantom to emulate vascular dementia pathologies. The reflection data was captured through RF sensors after each physical alteration in the artificial brain phantom. The backscattered signal data was used to reconstruct the brain atrophy and stroke images using different beamforming algorithms. The beamforming imaging is based on the difference in dielectric properties of the stroke and brain atrophy targets and the surrounding healthy tissues. The antenna sensors collect the reflected microwaves and the data is analyzed using customized state-of-the-art (SOTA) imaging algorithms. The imaging results from these confocal imaging algorithms are analyzed based on contrast, spatial resolution, noise suppression and computational complexity. These performance parameters are iteratively refined to develop an enhanced algorithm that offers an accurate imaging of stroke and atrophy ensuring optimal signal-to-noise ratio, contrast ratio and noise suppression. The modified SOTA algorithms are quantitatively compared with the proposed Double Stage Minimum Variance Delay and Sum (DS-MV-DAS) algorithm. Fig. 1 illustrates the overall architecture and design flow of the system. The proposed sensing and imaging system can detect and localize stroke and brain atrophy degeneration with high-resolution images.

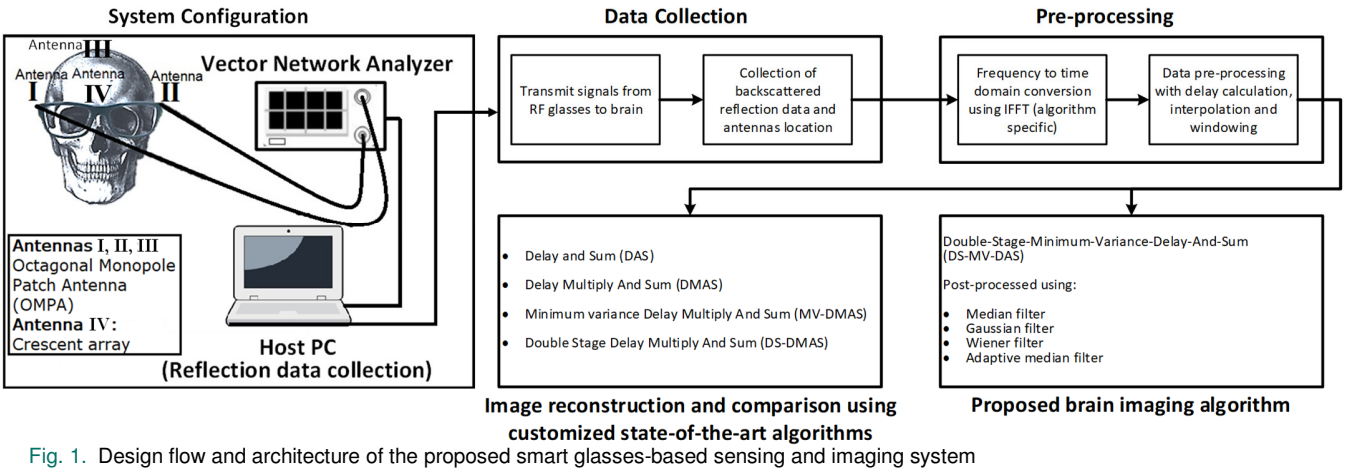

Fig. 1. Design flow and architecture of the proposed smart glasses-based sensing and imaging system

III. Sensor Design

Sensing and imaging of vascular dementia requires deep penetration of electromagnetic waves within the brain. Ultra-wideband (UWB) frequency can easily penetrate through the skull, and can precisely detect the pathophysiological degeneration within the brain [23]. Therefore, the antenna sensors are designed to operate on a UWB frequency range between 1 and 3 GHz, which ensures maximum coverage inside the brain. The UWB frequency band is more resistant to interference compared to the millimeter waves [24]. The penetration at the higher frequency decreases due to the increased scattering from the skull [25].

The octagonal monopole-patch antenna (OMPA) sensor is designed to scan the temporal and parietal regions of the brain. The proposed OMPA antenna sensor has dimensions of 50 x 80 mm^2 and is implemented on an FR4 substrate with a dielectric constant of 4.4 and a thickness of 1.6 mm. The designed antenna contains a single octagonal-shaped monopole radiating element that is fed with a 50 Ω feed line, as shown in Fig. 2 (a). The width of the feeding line is F_W = 3 mm and the length is F_L = 55 mm. The proposed octagonal design is derived from a rectangular patch antenna. The patch antenna and feedline are optimized to achieve the desired resonant frequency, uniform radiation pattern, high sensitivity and high impedance matching. Slots are introduced within a partial ground plane structure, which results in a wide bandwidth of 2 GHz, ranging from 1.5 GHz to 3 GHz, as shown in Fig. 5 (a). Edges of radiation elements are truncated to form an octagonal shape, which yields a compact structure and high impedance bandwidth. Symmetric circular slots and partial ground plane are introduced in the RF sensor structure to improve the bandwidth and reflection at lower frequencies. A rectangular slot in the middle of the ground plane helps to achieve wideband performance. Other dimensions of the antenna as shown in the schematic Fig. 2 (b) are W=50 mm, L=80 mm, G_L= 50 mm, G_W= 23.5 mm, S_L= 30 mm, S_W= 3 mm and S_R= 4 mm.

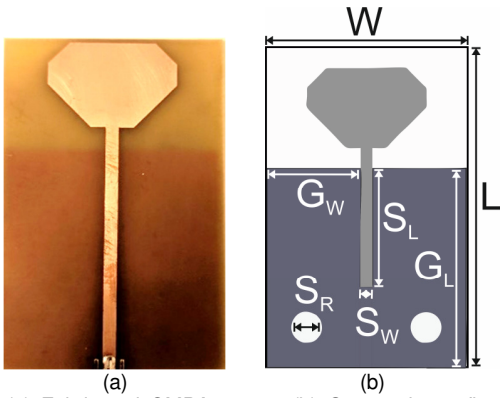

Fig. 2. (a) Fabricated OMPA sensor (b) Geometric configuration of proposed OMPA sensor

To ensure a complete brain scan, a 2x1 sensor array is designed to integrate with the front bridge of the glasses. The placement of the antenna array at the front and back of the head scans the frontal lobe, prefrontal cortex, and occipital lobe. The proposed antenna array has dimensions of 8 x 97 mm^2 and is implemented on an FR4 substrate with a dielectric constant of 4.4 and a thickness of 1.6 mm. Both antenna elements of the array are designed on a separate ground plane that is chamfered for bandwidth improvement. A crescent-shaped monopole antenna element is designed on each chamfered ground segment with a 50 Ω triangular tapered feed line, as shown in Fig. 3 (a). The length of the feeding line is F_L= 39 mm, and the width of the feeding line and feed port is F_{W1}= 3.2 mm and F_{W2}= 4.8 mm respectively. There is a spacing of 8 mm between antenna elements to reduce mutual coupling and improve isolation. Other dimensions of the antenna array as shown in the schematic Fig. 3 (b) are W_2= 18 mm, G_L= 10 mm, G_W= 8 mm, F_L= 39 mm, F_{W1}= 3.2 mm, F_{W2}= 4.8 mm, C_1, C_2= 3 mm, and D= 8 mm.

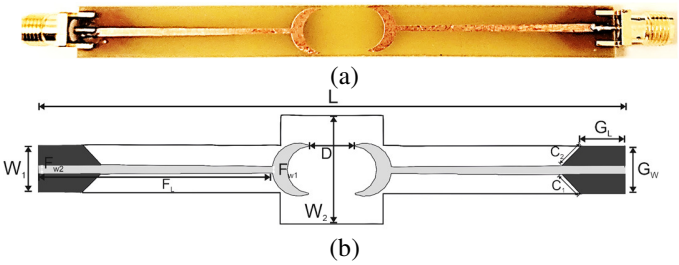

Fig. 3. (a) Fabricated crescent antenna array (b) Geometric configuration of proposed crescent antenna array

IV. Results

A. Software Simulation and Near-Field Analysis

The antenna sensors are designed optimized and computationally verified using CST Microwave Studio. A realistic brain voxel model [26] is used for near-field simulations, with brain elements including the skull, blood, cerebrospinal fluid, skin, grey and white matter, as shown in Fig. 4 (b). The designed OMPA sensor is integrated with left and right hinges and a crescent array is placed on the front bridge of the 3D glasses model, as illustrated in Fig. 4 (a). The sensors were initially validated on the baseline brain voxel to assess the radiation performance, directivity, efficiency and penetration on the operational frequency range between 1 GHz and 3 GHz. The three-dimensional (3D) radiation patterns of the OMPA and crescent array are presented in Fig. 5 (a) and Fig. 5 (b), respectively. Table I presents a comparative analysis between the proposed antennas and state-of-the-art wearable antennas. The proposed antennas are compact and offer high gain, bandwidth and efficiency as compared to the other antennas. Besides, OMPA sensor provides a directivity of 8.57 dB whereas the crescent array has a peak directivity of 4.43 dB. The OMPA and crescent array sensors achieve maximum simulated efficiencies of 77 % and 65%, respectively. A time-domain characterization was performed to analyze the impact of biological layers on the transmitted electromagnetic (EM) waves. The field probes were placed within the brain at a distance of 40 mm and 80 mm, and the EM pulse was transmitted into the brain. The backscattered pulse was collected by the sensor with a variable delay from the two field

TABLE I
PERFORMANCE COMPARISON WITH STATE-OF-THE-ART ANTENNAS

Feature	OMPA	Crescent array	[27]	[28]	[10]	[29]	[30]
Dimensions (mm)	50 x 80	8 x 97	122.5 x 122.5	36 x 39	20 x 66	300 x 360	38 x 76
Maximum Gain (dB)	7.8	5.6	7.2	4	_	3.5	3.5
Efficiency (%)	77	65	72	83	_	80	_
Frequency range (GHz)	1-2.5	1-3	2.25-2.75	2.4, 5.2, 5.8	1-6	0.94-2.7	1.1-1.3
Bandwidth (GHz)	1.5	2	0.5	_	1	1.75	0.2
Application	Vascular dementia	Vascular dementia	Wearable healthcare, WBANs	WLAN and WiMAX	Blood glucose detection	Brain stroke	Haemorrhagic stroke

probes, as shown in Fig. 5 (c) and Fig. 5 (d) for OMPA and crescent array sensors, respectively. After this validation, the dielectric properties of brain regions were modified to emulate stroke and brain atrophy. The reflection (S_{11}) data is collected for each degenerative pathology, stroke and atrophy target. The relative permittivity of grey matter was decreased from 54.8 to 41 for brain atrophy simulations. The dielectric permittivity of the white matter layer was reduced from 40.5 to 36.5. These changes characterize the accumulation of cerebrospinal fluid within the brain cavities and are based on the dielectric measurements of diseased brain tissue samples [31]. These values are taken as a reference for the simulation work performed on CST Microwave Studio with a realistic voxel model. Similarly, the permittivity of the blood pool was reduced from 63.2 to 56.5 for stroke analysis. The blood density was increased to 1190 kg/m^3 from an average blood density of 1060 kg/m^3 [32]. The reflection results for stroke and brain atrophy are presented in Fig. 5 (e) and Fig. 5 (f) for OMPA and crescent array sensors, respectively. The magnitude difference indicates the change in reflected power from a normal brain as compared to a brain with pathology. In the case of brain atrophy, the water content within cerebrospinal fluid results in higher absorption of the EM waves and results in lower reflected power at around 2.3 GHz. Similarly, the variation in relative permittivity and blood density leads to increased absorption within the stroke target. This results in lower S_{11} (dB) values for stroke as compared to the normal brain model.

The S_{11} measurements were taken with varying sensor-brain separation to assess the impact on the results. The measurements were recorded at 10 mm, 15 mm and 20 mm to investigate the optimal relative position for the sensors. The optimum results were achieved at a sensor-brain separation of 10 mm, as shown in Fig. 5 (g) and Fig. 5 (h) for OMPA and crescent array sensors, respectively. Due to this close proximity, the impact of sensors on the brain was also examined during the implementation phase. Specific Absorption Rate (SAR) is a primary criterion to evaluate the safety of antenna sensors as this measurement provides the safe amount of radiation absorbed by the body. The IEEE standard allows a maximum absorption of 1.6 W/Kg for 1g and the International Commission for Non-Ionizing Radiation Protection permits a maximum SAR of 2 W/Kg per 10g [33]. The maximum SAR for the OMPA sensor was 1.73 W/Kg (at input power of 100 mW), when the antenna was placed 10 mm away from the brain. The maximum SAR value for the crescent array was 1.18 W/Kg at 100 mW. The SAR was calculated at different points by varying the gap between the antenna and phantom, and recorded values are shown in Table II.

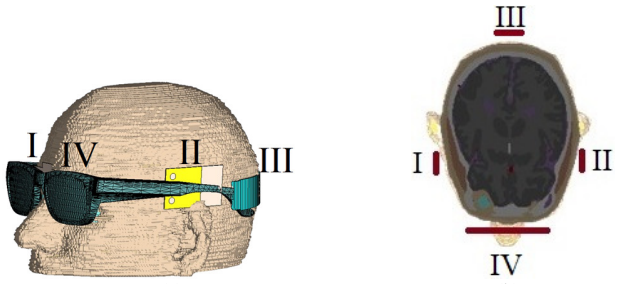

Fig. 4. (a) RF sensors placement on head voxel model for software simulations (b) Cross-sectional view of voxel model from top with brain entities and layers

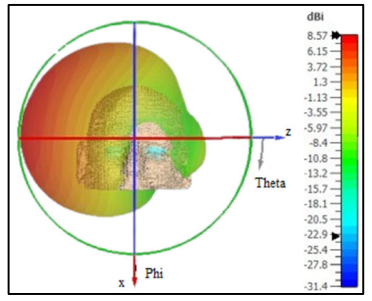

(a)

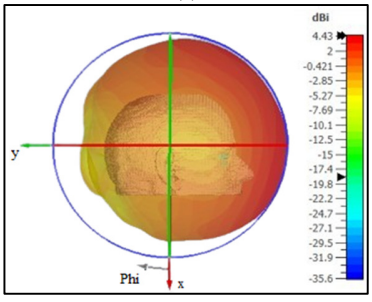

(b)

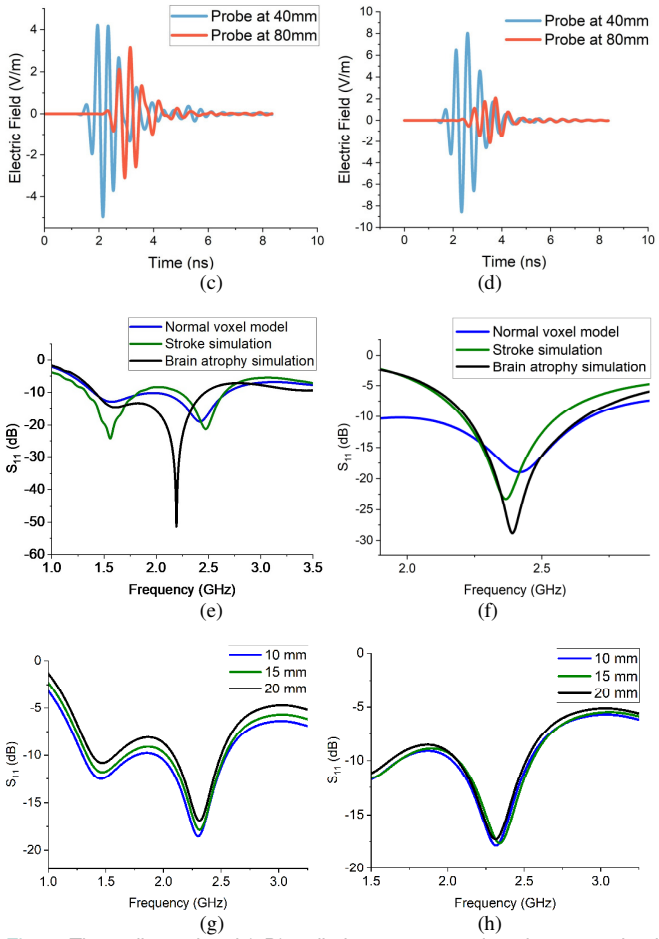

Fig. 5. Three dimensional (3D) radiation pattern against the customized head voxel model for (a) OMPA sensor (b) Crescent array; Simulated near-field pulses to verify the penetration at a distance of 40 mm and 80 mm inside brain phantom for (c) OMPA sensor (d) Crescent array; Reflection measurements (S_{11}) with simulated brain atrophy and stroke condition for (e) OMPA sensor (f) Crescent array; Antenna-head separation results for (g) OMPA sensor (h) Crescent array

TABLE II
SPECIFIC ABSORPTION RATE (SAR) OF ANTENNA SENSORS (PER 10G)

Sensor-phantom separation (mm)	OMPA sensor SAR (W/Kg)		Crescent array SAR (W/Kg)	
	10 mW	100 mW	10 mW	100 mW
10	0.171	1.73	0.119	1.18
15	0.145	1.59	0.079	1.11
20	0.139	1.42	0.062	0.97

As the sensors are designed to operate close to the brain, the effect of the RF sensors on tissue temperature is investigated. The temperature is measured at the skull, skin tissues, and gray and white matter layer of the brain. Thermal simulations are conducted using CST Studio thermal transient solver, which provided the average increase in temperature over the default brain voxel temperature of 36 °C. There is a minimal increase in temperature for white matter; the maximum temperature increase is at the skin. The OPMA sensors resulted in a maximum increase of 0.16 °C at the skin layer. The crescent array resulted in an increase of 0.132 °C at the skin, which is too minimal to have any adverse impact on the safety of the brain. The measured temperature values of other brain entities are presented in Table III.

TABLE III
TEMPERATURE INCREASE WITHIN BRAIN ENTITIES (CELSIUS)

Simulated Sensor	Skin	Skull	Gray matter	White matter
Sensor-I, II, III (OMPA)	0.16	0.15	0.14	0.13
Sensor-IV (Crescent Array)	0.13	0.12	0.11	0.09

B. Experimental Validation

The RF sensors were fabricated and verified on an artificial brain phantom with brain atrophy, blood clots and stroke target inside. The experimentation was done using RF sensors, a Vector Network Analyzer (VNA) and a PC with measurement software, as presented in Fig. 6. An HP 8753C VNA was used for experiments, with a frequency range of 300 kHz to 3 GHz and a dynamic range of up to 100 dB. The brain phantom was fabricated using a mixture of sugar, agar and water with an overall concentration of 1400 ml which closely matches the total brain volume of an average adult [34]. Dielectric properties of the phantom mixture were comparable to the real human brain, which were measured with an Agilent high-temperature dielectric probe 85070E-0020, as shown in Fig. 7 (a).

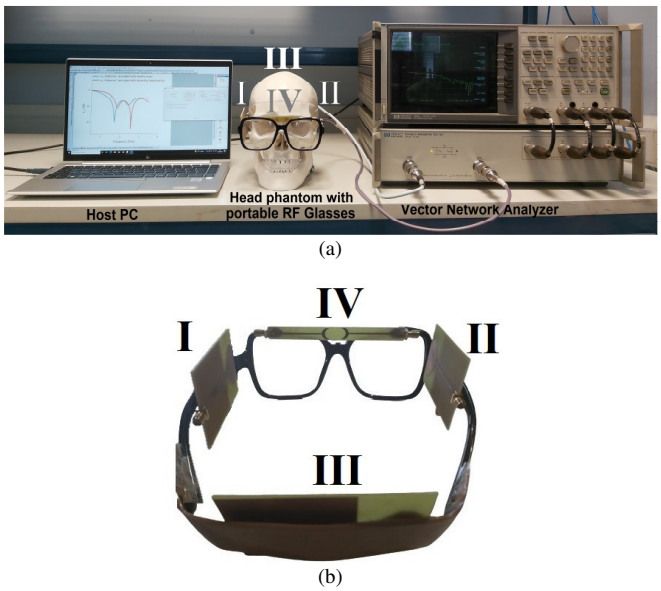

Fig. 6. (a) Experimental setup with VNA, laptop, head phantom, and smart RF glasses (b) Geometry of the glasses highlighting placement of RF sensors

The proposed RF sensing system was first verified on a normal brain phantom placed inside the skull model, as shown in Fig. 7 (b). Reflection measurements (S_{11}) were initially taken with a normal brain model as a reference benchmark. This reference dataset was helpful in the image reconstruction for both experimental cases of vascular dementia: stroke and brain atrophy. The artificial stroke and blood clot target was emulated using a shallow spherical target with a volume of 27 mm^3, as shown in Fig. 7 (c). This spherical ischemic target was filled

with saline liquid to match the dielectric constant of an actual blood clot [35]. The dielectric permittivity of the stroke target is around 69, compared to the permittivity of 63 for the brain matter. The target was placed in the middle of the brain phantom to create an artificial brain stroke scenario. Reflection measurements (S_{11}) were taken with RF glasses placed around the head phantom. There was a strong reflection in the presence of the stroke target, as compared to the normal brain, as shown in Fig. 8 (a) and Fig. 8 (c) for OMPA and crescent sensor array respectively. This strong reflection is due to the dielectric contrast between the saline-filled spherical and the surrounding brain tissues.

The brain atrophy is emulated using a modified brain phantom. The brain matter is altered by the removal of the stroke target and the fabrication of a cavity with a volume of 38 mm^3 in the middle of the brain matter. The cavity was filled with a mixture of water, salt, coconut oil, and agar to represent the cerebrospinal fluid (CSF) accumulation inside [36]. The dielectric properties of the CSF material were measured with a dielectric probe, at each step of mixture preparation, to keep it consistent with the dielectric properties of the actual diseased brain tissues [31]. The measured dielectric permittivity of the fabricated CSF material was around 55 in contrast to the dielectric permittivity of 63 for the brain matter. The results were taken with RF glasses and a noticeable reflection from CSF can be seen in Fig. 8 (b) and Fig. 8 (d) for OMPA and crescent sensor array, respectively. The increased reflection is due to the dielectric properties of the CSF mixture differing from the surrounding brain matter. As the CSF is more conductive due to higher water content and lower cellular composition, the accumulation of CSF in the atrophy region contributes to the changes in the dielectric properties of pathological tissue [37]. These pathological changes including accumulation of CSF in case of brain atrophy affect the relative permittivity and result in dielectric contrast that leads to the variations in reflected signals as shown in Fig. 8. The reflection data collected by the RF sensors is utilized for image reconstruction, which further supports visualizing the differences between healthy and diseased brain tissue. For image reconstruction, additional measurements were taken from the back of the head by placing the OMPA sensor on an extended headband to reconstruct images, as shown in Fig. 6 (b).

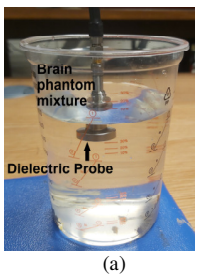

(a)

(b)

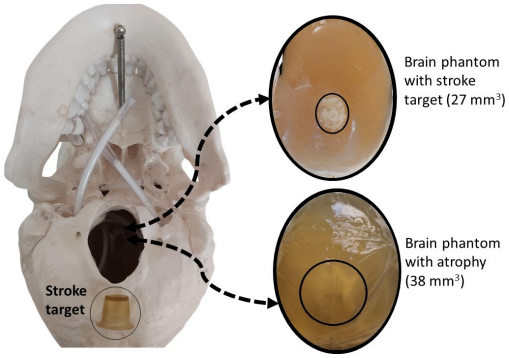

(c)

Fig. 7. (a) Dielectric measurement of brain phantom material with dielectric probe (b) Fabricated brain phantom with skull (c) Fabricated artificial brain phantom with stroke and brain atrophy targets

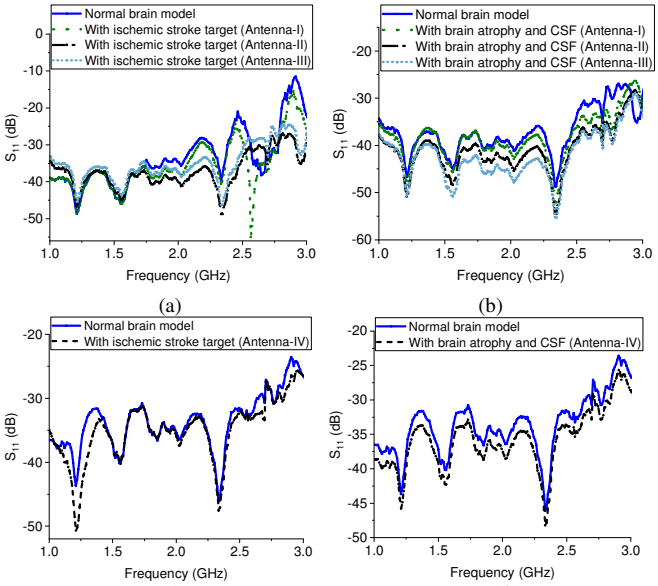

Fig. 8. Reflection (S_{11}) measurements from OMPA antenna-I, II, III for (a) ischemic stroke target (b) brain atrophy; Reflection (S_{11}) measurements from crescent array antenna-IV for (c) ischemic stroke target (d) brain atrophy

To evaluate the repeatability and reproducibility, an additional set of measurements was taken from both OMPA and crescent array sensors with the baseline brain model. The mean and standard deviation of these measurements are utilized to calculate the percentage coefficient of variation. The coefficient of variation (CV) provides a normalized measure of dispersion to compare the degree of variation between the measurements and can be calculated as the ratio of standard deviation to the mean. The CV values for the OMPA and crescent sensor are 5.8% and 6.7% respectively, which indicates high precision and tolerance for variability. Fig. 9 (a) and Fig. 9 (b) illustrate the consistency in measurements for the OMPA sensor and crescent array sensor, respectively. The box plot presents the distribution summary of each measurement set, highlighting median S_{11} (dB), quartiles and outliers. This provides a visual assessment of the consistency in measurements across different sets. Furthermore, the S_{11} (dB) measurements are presented for each set of measurements, which indicates the consistent

measurements across sets, mapped against the operating frequency (GHz).

Furthermore, the reproducibility of the measurements is analyzed using the analysis of variance (ANOVA) test. The ANOVA test provides an F-statistic and a p-value, which are utilized to examine the differences between the set of measurements. The F-statistic is a ratio of the variance between the measurement sets to the variance within the measurement set. The p-value indicates whether the differences in measurements are statistically significant to reject the null hypothesis [38]. The [F-value, p-value] for the set of measurements taken with OMPA and crescent array sensor are [0.042, 0.99] and [0.003, 0.98], respectively. The lower F-values suggest that the variance between the set of measurements is small compared to the variability within each measurement set. The high p-value, greater than 0.05, for both the sensor measurements indicates that there is no statistically significant difference between the measurement sets.

The measurement uncertainty is evaluated according to the Guide to the Expression of Uncertainty in Measurement (GUM) [39]. The acceptable uncertainty for RF sensing applications is generally between ± 0.1 dB and ± 1 dB [40]. The combined standard uncertainty is calculated based on the statistical analysis of the repeated set of measurements. The expanded uncertainty is calculated with a coverage factor of 2, which implies that the true value is expected in the range with 95% confidence. The combined standard uncertainty for the measurements taken with OMPA and crescent array sensor are ± 0.31 dB and ± 0.17 dB, respectively. The expanded uncertainty values are ± 0.42 dB and ± 0.25 dB for OMPA and crescent array sensor, respectively. The acceptable deviation for wearable biomedical sensing applications is upto ±1 dB to ensure reliable and accurate sensor performance. The proposed sensors consistently provide measurements within this acceptable deviation range, confirming their stability and accuracy.

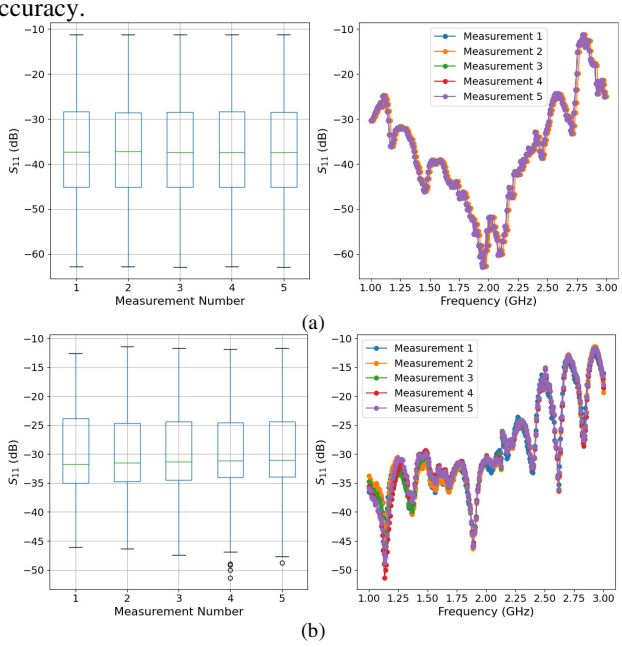

Fig. 9. Reflection (S_{11}) measurements taken with baseline brain model to evaluate the repeatability and reproducibility of measurements for (a) OMPA antenna-I, II, III (b) crescent array antenna-IV

C. Microwave Imaging Algorithms for Brain Image Reconstruction

The proposed imaging system is evaluated using customized confocal microwave imaging algorithms. The reflection measurements from the experimentation were utilized to recreate images of anomalies for both brain stroke and brain atrophy. In addition to the glasses, an antenna sensor was deployed around the back of the head for complete coverage of the brain phantom and to accurately reconstruct the images. This was done by using a headband integrated with wearable glasses. The location of four antennas was defined at (50, 0), (50, 100), (0, 50), (100, 50) according to the axis shown in Fig. 10. The location coordinates are in millimeters and the resultant images are scaled to represent the actual anatomical dimensions of an average human head. These scaling adjustments during post-processing improve the visual representation of the brain and keep the imaging anatomically consistent. The collected backscattered signal data is preprocessed for image reconstruction through MATLAB. The data utilized for imaging of stroke and atrophy pathology included the reflection (S_{11}) measurements on 300 frequency points over the frequency range from 1 to 3 GHz. The measured data is converted to magnitude from decibel (dB) values, before processing it with the customized beamforming imaging techniques.

The backscattered RF data is initially analyzed through customized SOTA imaging algorithms. These algorithms are specially modified in this work to reconstruct brain images through the coherent addition of backscattered signals. The data collected from the sensors is pre-processed, time-aligned, and interpolated and the images are constructed through these beamforming algorithms. The reflection data is initially processed using a customized Delay and Sum (DAS) beamforming algorithm. The reflected microwave signals are time-aligned and interpolated to reconstruct the energy distribution and mapped into a two-dimensional image. The output of the DAS beamformer can be represented with (1):

$$z_{DAS}(t) = \sum_{i=1}^{n} x_i(\mathrm{t} - \Delta_i) \qquad (1)$$

Where $z_{DAS}(t)$ is the output of DAS, t is the time index, n is the number of antenna elements and $x_i(\mathrm{t})$ is the detected signal with the equivalent time delay Δ_i. The DAS-constructed images for stroke and brain atrophy are presented in Fig. 10 (a) and Fig. 11 (a), respectively. The spherical stroke target with a volume of 27 mm^3 was placed in the middle of the brain phantom and the affected area is visible in the center of the heat map. The brain atrophy target is fairly spread out due to a wider cavity of 38 mm^3, with the red region indicating the atrophy and the yellow zone representing the cerebrospinal fluid. Although the reconstructed images are accurate with the location of target anomalies, the resultant images are low resolution and the side lobes in the beam pattern result in imaging artifacts. The spatial and contrast resolution is low due to limited noise suppression by the DAS beamforming. As the high level of side lobes

significantly degraded the quality of the image reconstructed using DAS, the backscattered data is processed using a specialized Delay Multiply and Sum (DMAS) algorithm for the proposed imaging device. The DMAS imaging algorithm is an advanced variation of DAS that incorporates an additional signal multiplication. The time-aligned signals from each antenna element are multiplied by their complex conjugates or envelope-detected versions. This results in a phase correction, which effectively enhances the coherent component of the signals while suppressing the noise, clutter and incoherent components. This leads to a more accurate localization of stroke and brain atrophy targets. The beamformer output for DMAS is given by (2).

$$z_{DMAS}(t) = \sum_{i=1}^{n-1} \sum_{j=i+1}^{n} x_i(t)\, x_j(t) \qquad (2)$$

Where $z_{DMAS}(t)$ is the output of the DMAS beamformer, t is the time-index, n is the number of antenna elements, $x_i(t)$ and $x_j(t)$ are the delayed detected signals for i^{th} and j^{th} elements, respectively. The reconstructed DMAS images for stroke and brain atrophy are presented in Fig. 10 (b) and Fig. 11 (b), respectively. The customized Minimum Variance Delay Multiply and Sum (MV-DMAS) algorithm combines adaptive weights, delay, signal multiplication and summation. The resulting image quality is improved by minimizing variance and enhancing the coherent signal components. The output of the MV-DMAS beamformer can be represented using (3).

$$z_{MV-DMAS}(t) = \frac{1}{n} \sum_{i=1}^{n-1} \sum_{j=i+1}^{n} z_i(t)\, z_j(t) \qquad (3)$$

Where $z_i(t)$ is the output of the single MV-DMAS beamforming signal, and can be represented using (4).

$$z_i(t) = w_{rx}^H s_{rx_i}(t) \qquad (4)$$

Here, s_{rx_i} denotes the received backscattered signals, w_{rx} is the weight of received signals that are used to calculate the covariance matrix using (5).

$$R_{rx}(t) = \frac{1}{n} \sum_{i=1}^{n} R_{rx,i}(t) \qquad (5)$$

Where $R_{rx,i}(t)$ represents the covariance matrix to de-correlate the signals using spatial smoothing and is represented using (6). Where n represents the number of antenna elements and m is the length of the antenna array for spatial averaging.

$$R_{rx,i}(t) = \frac{1}{n-m+1} \sum_{y=1}^{n-m+1} x_y(t)\, x_y^H(t) \qquad (6)$$

MV-DMAS beamforming provides an improved contrast with effective noise suppression, as shown in Fig. 10 (c) and Fig. 11 (c) for ischemic stroke and brain atrophy respectively. MV-DMAS is sensitive to the accuracy of the statistical covariance and variance matrices, and slight deviations may result in image artifacts and misalignments. The stroke and brain atrophy reflection data are further analyzed using the Double Stage Delay Multiply and Sum (DS-DMAS) algorithm. The algorithm provides an improved image quality and spatial resolution through iterative refinement. This involves a two-stage delay, summation and multiplication to enhance the coherent components of the microwave signals. The DS-DMAS beamformer can be represented by (7).

$$z_{DS-DMAS}(t) = \sum_{i=1}^{n-2} \sum_{j=i+1}^{n-1} x_i(t)\, x_j(t) \qquad (7)$$

Where $z_{DS-DMAS}(t)$ is the output of the DS-DMAS beamformer, t is the time-index, n is the number of antenna elements, $x_i(t)$ and $x_j(t)$ are the delayed detected signals for i^{th} and j^{th} elements, respectively. The images constructed through DS-DMAS for ischemic stroke and brain atrophy are presented in Fig. 10 (d) and Fig. 11 (d), respectively. The noise suppression results in refined sharp images as compared to DAS and DMAS.

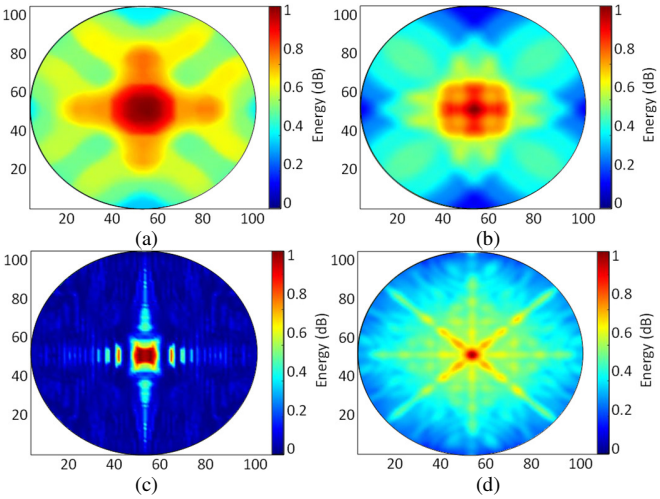

Fig. 10. Reconstructed images for ischemic stroke with (a) Delay-And-Sum (DAS) (b) Delay-Multiply-And-Sum (DMAS) (c) Minimum Variance Delay-Multiply-And-Sum (MV-DMAS) (d) Double-Stage Delay-Multiply-And-Sum (DS-DMAS)

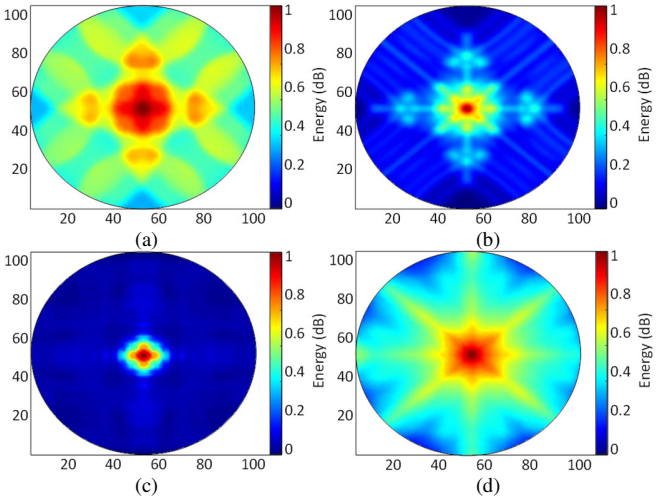

Fig. 11. Reconstructed images for brain atrophy with (a) Delay-And-Sum (DAS) (b) Delay-Multiply-And-Sum (DMAS) (c) Minimum Variance Delay-Multiply-And-Sum (MV-DMAS) (d) Double-Stage Delay-Multiply-And-Sum (DS-DMAS)

D. Proposed Imaging Algorithm and Comparative Performance Analysis

Based on image quality, computational complexity and noise suppression, the optimal result is achieved through the customized Minimum Variance Delay Multiply and Sum (MV-DMAS). Although MV-DMAS provided an accurate image reconstruction of stroke and brain atrophy, the contrast resolution can be further enhanced using a multi-stage variant of MV-DMAS. Based on imaging analysis with SOTA algorithms, the novel Double Stage Minimum Variance Delay Multiply and Sum (DS-MV-DMAS) algorithm is proposed, which is carefully optimized to ensure a balance between noise suppression and computational complexity. Since the data is processed from only four antenna sensors, we can trade off computational demand with the imaging quality. Due to the lower count of antenna elements, the overhead computational cost will not affect the proposed imaging device.

The proposed DS-MV-DMAS algorithm introduces a two-stage processing approach after data acquisition, adaptive weighing, delay, and signal multiplication and summation process, as illustrated in Fig. 12. The process initiates by reading the antenna location around the head phantom. The head imaging requires the position of antennas to be updated according to the circumference of the head. This initial algorithm block assists in calculating the time shift for the backscattered signals to match the distance to the sensors' placement coordinates on the head. The first stage involves the calculation of the covariance matrix for the backscattered signals from all antenna elements. The adaptive minimum variance (MV) weight factors are calculated based on the covariance matrix to enhance the coherent signal components, as given in (6). The received signals are time-aligned and multiplied by their complex conjugates. This is followed by the summation of the multiplied form of beamformed signals for each imaging point. The second stage is similar to the first stage and provides an enhanced refinement of beamformed signals.

The dual-stage process results in an improved image contrast, reduced variance, and enhanced coherent signal components. To further improve the image quality, four different filters were investigated to incorporate with the proposed Double Stage Minimum Variance Delay Multiply and Sum (DS-MV-DMAS) algorithm: Median filter, Gaussian filter, Wiener filter and Adaptive median filter. The median filter removes the low-intensity image pixels by replacing each pixel value with the median of the neighboring pixel. A customized 5x5 median filter is used to post-process the stroke and brain atrophy data. The post-processed images are presented in Fig. 13 (a) and Fig. 14 (a) for stroke and brain atrophy, respectively. The DS-MV-DMAS with median filter provides an improved heat map for the reconstructed images, as compared to other SOTA algorithms implemented in this work.

The output of the proposed algorithm is then post-processed using a Gaussian filter, which performs a weighted average of the surrounding pixels based on Gaussian distribution. As compared to the median filter, post-processing with a Gaussian filter provides an improved contrast resolution. However, the low energy components are noticeable including the reflection from antenna elements, as shown in Fig. 13 (b) and Fig. 14 (b). The DS-MV-DMAS beamformed data is subsequently post-processed through a Wiener filter of a 5x5 window and the results are presented in Fig. 13 (c) and Fig. 14 (c) for stroke and brain atrophy, respectively. The Wiener filter is commonly used to remove additive noise through linear estimation of the original image. The low noise components are blurred as compared to the Gaussian filter, but the target anomalies are not spectrally enhanced. This is because Weiner filters are unable to reconstruct original frequency components already degraded by noise.

As the median filter provided enhanced images for stroke and atrophy, the results are post-processed with an adaptive median filter. The adaptive mean filter performs spatial processing to determine the pixels affected by noise components. Unlike the median filter, the adaptive median filter preserves detail and neutralizes non-impulsive noise. An adaptive median filter with a window size of two is used to post-process the data, with an incremental window size of two on each iteration. The maximum window size is six for the proposed filtering. Resultantly, the low noise components are counterbalanced but the reflection from antenna elements is comparatively highlighted in this case. The results are presented in Fig. 13 (d) and Fig. 14 (d) for stroke and atrophy, respectively. Based on these results, the median filter outperforms the other filters in terms of noise cancellation and spectral enhancement.

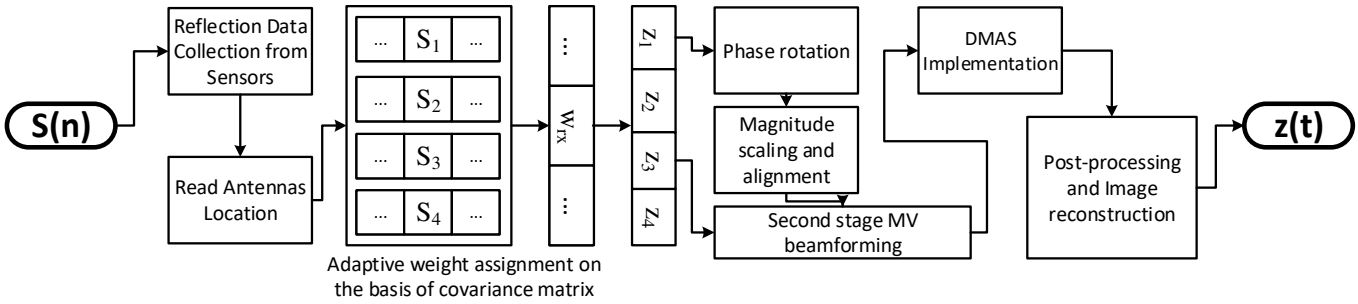

Fig. 12. Process flowchart of the proposed Double Stage Minimum Variance Delay Multiply and Sum (DS-MV-DMAS) algorithm

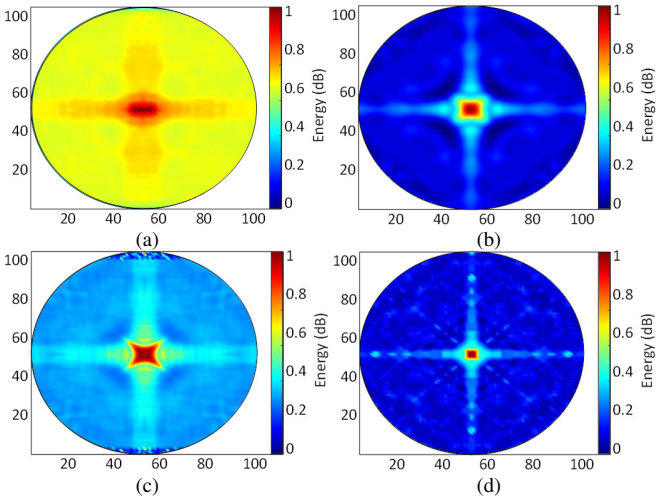

Fig. 13. Reconstructed stroke images with proposed Double-Stage-Minimum-Variance-Delay-Multiply-And-Sum (DS-MV-DMAS) (a) with median filter (b) with Gaussian filter (c) with Wiener filter (d) with an adaptive median filter

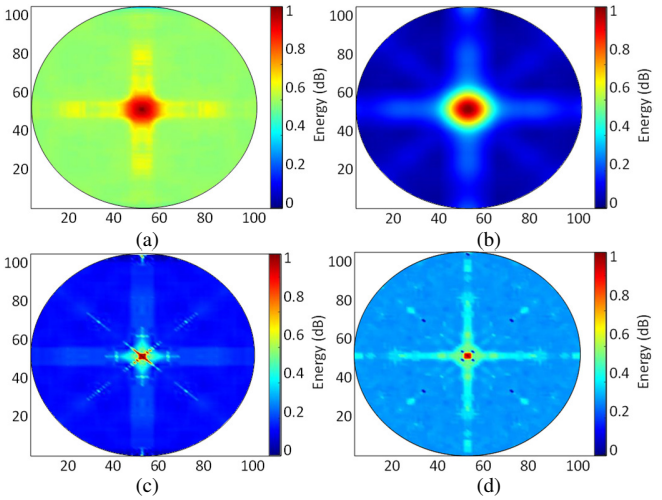

Fig. 14. Reconstructed brain atrophy images with proposed Double-Stage-Minimum-Variance-Delay-Multiply-And-Sum (DS-MV-DMAS) (a) with median filter (b) with Gaussian filter (c) with Wiener filter (d) with an adaptive median filter

The performance of proposed DS-MV-DMAS algorithm is further verified with placement of stroke and atrophy targets at off-centre locations, as illustrated in Fig. 15. Target A is placed on top left and target B is added on bottom right of the phantom. Similar to the fabricated model shown in Fig. 7, the stroke target is emulated by a shallow spherical target with volume of 27 mm^3. For brain atrophy, the brain matter is altered by the removal of the stroke target and the fabrication of cavity with a volume of 38 mm^3. The cavity was then filled with a mixture of water, salt and agar to represent the cerebrospinal fluid (CSF) accumulation inside. The measurements are taken for each target after modifications in the brain phantom.

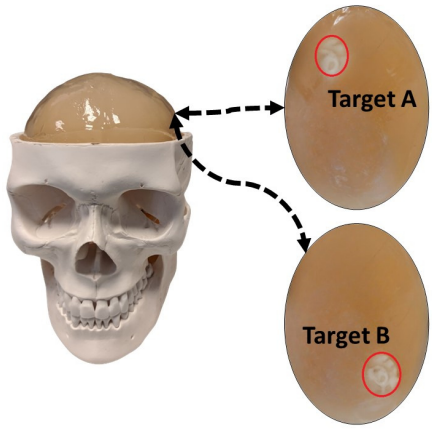

Fig. 15. Modified fabricated brain phantom illustrating the locations of off-center stroke and brain atrophy targets

The results are processed using the proposed DS-MV-DMAS to assess the efficacy of the imaging system in detection of off-centre targets. The output of DS-MV-DMAS is post-processed using the median filter as it provided an optimal performance in terms of noise cancellation and spectral enhancement, as compared to other filters. The results of target A are presented in Fig. 16 (a) and Fig. 16 (b) for stroke and atrophy, respectively. For target B, the results are presented in Fig. 16 (c) and Fig. 16 (d) for stroke and atrophy, respectively.

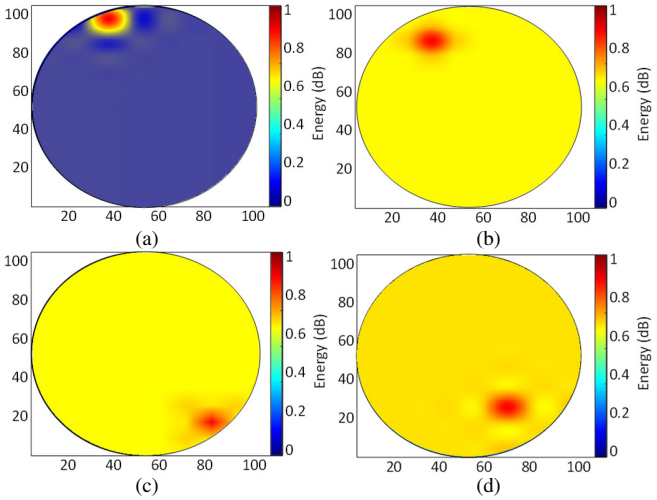

Fig. 16. Reconstructed brain atrophy images with proposed Double-Stage-Minimum-Variance-Delay-Multiply-And-Sum(DS-MV-DMAS) with median filter for (a) stroke target A (b) atrophy target A (c) stroke target B (d) atrophy target B

The performance of algorithms is quantitatively analyzed, and compared with the proposed algorithm. The evaluation metrics included Signal-to-Noise Ratio (SNR), Contrast Ratio (CR), Full Width at Half Maximum (FWHM) and percentage of side lobes. The analysis is performed using MATLAB. The performance of algorithms is quantitatively analyzed, and compared with the proposed algorithm.

The evaluation metrics included Signal-to-Noise Ratio (SNR), Contrast Ratio (CR), Full Width at Half Maximum (FWHM) and percentage of side lobes. The analysis is performed using MATLAB. Signal-to-Noise Ratio (SNR) is computed using the average signal data from the four antennas,

TABLE IV
QUANTITATIVE COMPARISON OF PROPOSED DS-MV-DMAS ALGORITHM WITH CUSTOMIZED STATE-OF-THE-ART IMAGING ALGORITHMS

Imaging Algorithm	Signal-to-Noise Ratio (dB)		Contrast Ratio (dB)		Full Width at Half Maximum (mm)		Peak side lobe level (dB)	
	Stroke	Brain atrophy	Stroke	Brain atrophy	Stroke	Brain atrophy	Stroke	Brain atrophy
Delay and Sum (DAS)	9.7	11.5	0.28	0.34	0.6	0.6	-23.3	-25.8
Delay Multiply and Sum (DMAS)	15.2	17.6	0.39	0.48	0.6	0.5	-25.8	-29.6
Minimum Variance Delay Multiply and Sum (MV-DMAS)	28.9	29.6	0.69	0.71	0.5	0.4	-27.3	-38.4
Double Stage Delay Multiply and Sum (DS-DMAS)	29.2	31.5	0.72	0.75	0.5	0.4	-19.6	-22.5
Double Stage Minimum Variance Delay Multiply and Sum (DS-MV-DMAS) – Proposed	32.4	37.6	0.832	0.845	0.3	0.3	-32.4	-47.9

for both stroke and brain atrophy separately. The original reflection data from a normal brain phantom is used as a ground truth for the calculation of SNR. The SNR is calculated using (8), where P_S is the signal power of the scattering target and P_N denotes the power for the feature-free region.

$$SNR = 10\ \log_{10}\ \frac{P_S}{P_N} \tag{8}$$

This provides a quantitative comparison between maximum and minimum power intensities for each region. Table IV lists the calculated SNRs for each algorithm. The proposed DS-MV-DMAS algorithm improves the SNR by 26 dB compared with DAS. There is an SNR improvement of 8 dB and 6 dB in comparison to the MV-DMAS and DS-DMAS, respectively. The proposed algorithm provides an overall 43% reduction in side lobes, which improves the image quality. The DS-MV-DMAS algorithm leads to a reduction of 22 dB and 9 dB in the peak side lobe for brain atrophy and stroke, respectively, as compared to DAS.

The proposed algorithm achieves a 28% reduction in Full Width at Half Maximum (FWHM), which represents a considerable improvement in the spatial response of the imaging system. The FWHM represents the angular range on which the sensitivity of the proposed system is at least half of its maximum value. The FWHM of the system with DS-MV-DMAS is 0.3, compared to 0.5 and 0.4 for DMAS and MV-DMAS respectively, which implies a better spatial resolution. The reduction in FWHM normally results in higher side lobe levels, but the proposed algorithm maintains a balance by minimizing side lobe levels to avoid image artifacts. The FWHM values are presented in Table IV for stroke and brain atrophy. There is a maximum improvement of 27% in Contrast Ratio (CR) for DS-MV-DMAS, compared to other SOTA imaging algorithms [13][41]. The contrast ratio provides a distinguishability in features of the beamformed image. This is calculated through the difference in mean image intensities between the target regions of interest, using (9).

$$CR = 20\ \log_{10}\ \frac{|P_{max}| - |P_{\min}|}{|P_{max}| + |P_{min}|} \tag{9}$$

Where, P_{max} represents the maximum intensity region and P_{min} is the minimum intensity region. A higher value of contrast ratio leads to improved image quality and better visualization of degenerative pathologies. The calculated values of CR are presented in Table IV. The higher contrast ratio for DS-MV-DMAS validates the ability of the proposed algorithm to distinguish different regions for stroke and atrophy effectively.

V. CONCLUSION

An innovative smart RF glasses-based system is presented for the detection and imaging of vascular dementia. The proposed system can detect stroke and brain atrophy with high precision. The system is supported with a customized beamforming algorithm for high-resolution image reconstruction. The design of Ultra-wideband antenna sensors is optimized through software simulations with post-verification on head voxel models. Experimental validation of sensors is carried out by developing a realistic head phantom with brain atrophy and stroke anomalies. The measured results are post-processed with customized state-of-the-art imaging algorithms and the findings are utilized to design an improved algorithm that offers a high signal-to-noise ratio, high contrast resolution and low level of side lobes. The portability, cost-effectiveness and non-invasive design make this a novel system for medical diagnostics and imaging applications. Experimental results confirm the capability of this imaging system for early detection of neurodegeneration and the prototype device can be safely utilized for preclinical studies. These preclinical trials will consider individual calibration, baseline measurements, physiological factors and adaptive signal processing to compensate for individual variability. Ongoing research is focused on real-time data transmission, processing and imaging of the acquired data that could be beneficial for robust imaging, including with the use of machine learning approaches.

Future work will focus on the portability of the measurement setup, which includes an integrated analyzer and cloud data transfer. As this device is designed to integrate with the next-generation multimodal hearing aids, power optimization will be crucial to extend the battery life of the device. To regulate the power consumption, the sensing glasses will be integrated with a proximity sensor that will control the output of RF antennas through a portable Vector Network Analyzer (VNA). The portable VNA will be integrated with the headband around the back of the head. This subsystem will activate the sensing when the glasses are being worn by the patient and will switch off the VNA if the glasses are removed. This work is being carried out as a part of future integration. Furthermore, future research will focus on AI-assisted individualized calibration for personalized imaging. This approach will utilize machine learning algorithms to analyze initial scans and continuously adjust the sensors for optimal performance, enhancing the precision of the brain imaging process.

ACKNOWLEDGMENT

The authors would like to acknowledge the financial support of the Higher Education Commission, Pakistan and the UK Engineering and Physical Sciences Research Council (EPSRC) funded COG-MHEAR research program (Grant ref. EP/T021063/1). We are grateful to Mr. Iain Gold for his support and assistance in sensor fabrication.

REFERENCES

[1] F. J. Wolters and M. Arfan Ikram, "Epidemiology of Vascular Dementia: Nosology in a Time of Epiomics," *Arterioscler. Thromb. Vasc. Biol.*, vol. 39, no. 8, pp. 1542–1549, 2019, doi: 10.1161/ATVBAHA.119.311908.

[2] S. C. Bir, M. W. Khan, V. Javalkar, E. G. Toledo, and R. E. Kelley, "Emerging Concepts in Vascular Dementia: A Review," *J. Stroke Cerebrovasc. Dis.*, vol. 30, no. 8, p. 105864, 2021, doi: 10.1016/j.jstrokecerebrovasdis.2021.105864.

[3] U. Anwar, T. Arslan, A. Hussain, and P. Lomax, "Next Generation Cognition-Aware Hearing Aid Devices With Microwave Sensors: Opportunities and Challenges," *IEEE Access*, vol. 10, no. July, pp. 82214–82235, 2022, doi: 10.1109/ACCESS.2022.3195875.

[4] A. Brodtmann, M. S. Khlif, N. Egorova, M. Veldsman, L. J. Bird, and E. Werden, "Dynamic Regional Brain Atrophy Rates in the First Year after Ischemic Stroke," *Stroke*, no. September, pp. 183–192, 2020, doi: 10.1161/STROKEAHA.120.030256.

[5] J. D. Oldan, V. L. Jewells, B. Pieper, and T. Z. Wong, "Complete evaluation of dementia: PET and MRI correlation and diagnosis for the neuroradiologist," *Am. J. Neuroradiol.*, vol. 42, no. 6, pp. 998–1007, 2021, doi: 10.3174/ajnr.A7079.

[6] E. Soleimani, M. Mokhtari-Dizaji, N. Fatouraee, and H. Saberi, "Assessing the blood pressure waveform of the carotid artery using an ultrasound image processing method," *Ultrasonography*, vol. 36, no. 2, pp. 144–152, 2017, doi: 10.14366/usg.16019.

[7] S. Fantini, A. Sassaroli, K. T. Tgavalekos, and J. Kornbluth, "Cerebral blood flow and autoregulation: current measurement techniques and prospects for noninvasive optical methods," *Neurophotonics*, vol. 3, no. 3, p. 031411, 2016, doi: 10.1117/1.nph.3.3.031411.

[8] M. Baghelani, Z. Abbasi, M. Daneshmand, and P. E. Light, "Noninvasive Microwave Sensor for Real-Time Continuous Dehydration Monitoring," *IEEE Sens. J.*, vol. 24, no. 7, pp. 9959–9969, 2024, doi: 10.1109/JSEN.2024.3362702.

[9] S. Wang, W. Wang, and Y. Zheng, "Reconfigurable Multimode Microwave Sensor with Resonance and Transmission Sensing Capabilities for Noninvasive Glucose Monitoring," *IEEE Trans. Microw. Theory Tech.*, vol. 72, no. 5, pp. 3102–3117, 2024, doi: 10.1109/TMTT.2023.3324432.

[10] A. E. Omer *et al.*, "Non-Invasive Real-Time Monitoring of Glucose Level Using Novel Microwave Biosensor Based on Triple-Pole CSRR," *IEEE Trans. Biomed. Circuits Syst.*, vol. 14, no. 6, pp. 1407–1420, 2020, doi: 10.1109/TBCAS.2020.3038589.

[11] J. C. Chiao *et al.*, "Applications of Microwaves in Medicine," *IEEE J. Microwaves*, vol. 3, no. 1, pp. 134–169, 2023, doi: 10.1109/JMW.2022.3223301.

[12] A. Yan, L. Lin, C. Liu, J. Shi, S. Na, and L. V. Wang, "Microwave-induced thermoacoustic tomography through an adult human skull," *Med. Phys.*, vol. 46, no. 4, pp. 1793–1797, 2019, doi: 10.1002/mp.13439.

[13] R. Ullah, I. Saied, and T. Arslan, "Measurement of whole-brain atrophy progression using microwave signal analysis," *Biomed. Signal Process. Control*, vol. 71, no. PA, p. 103083, 2022, doi: 10.1016/j.bspc.2021.103083.

[14] A. Zamani and A. Abbosh, "Hybrid Clutter Rejection Technique for Improved Microwave Head Imaging," *IEEE Trans. Antennas Propag.*, vol. 63, no. 11, pp. 4921–4931, 2015, doi: 10.1109/TAP.2015.2479238.

[15] M. T. Islam, M. Z. Mahmud, M. T. Islam, S. Kibria, and M. Samsuzzaman, "A Low Cost and Portable Microwave Imaging System for Breast Tumor Detection Using UWB Directional Antenna array," *Sci. Rep.*, vol. 9, no. 1, pp. 1–13, 2019, doi: 10.1038/s41598-019-51620-z.

[16] D. O. Rodriguez-Duarte *et al.*, "Experimental validation of a microwave system for brain stroke 3-d imaging," *Diagnostics*, vol. 11, no. 7, pp. 1–18, 2021, doi: 10.3390/diagnostics11071232.

[17] L. Alon and S. Dehkharghani, "A stroke detection and discrimination framework using broadband microwave scattering on stochastic models with deep learning," *Sci. Rep.*, vol. 11, no. 1, pp. 1–9, 2021, doi: 10.1038/s41598-021-03043-y.

[18] A. T. Mobashsher, A. Mahmoud, and A. M. Abbosh, "Portable Wideband Microwave Imaging System for Intracranial Hemorrhage Detection Using Improved Back-projection Algorithm with Model of Effective Head Permittivity," *Sci. Rep.*, vol. 6, no. November 2015, pp. 1–16, 2016, doi: 10.1038/srep20459.

[19] U. Anwar, T. Arslan, A. Hussain, and P. Lomax, "Wearable RF Sensing and Imaging System for Non-invasive Vascular Dementia Detection," *2023 IEEE Int. Symp. Circuits Syst.*, vol. 1, pp. 4–8, doi: 10.1109/ISCAS46773.2023.10181959.

[20] "COG-MHEAR, EPSRC United Kingdom." [Online]. Available: https://cogmhear.org/

[21] H. F. Wang *et al.*, "Hearing impairment is associated with cognitive decline, brain atrophy and tau pathology," *eBioMedicine*, vol. 86, no. 12, p. 104336, 2022, doi: 10.1016/j.ebiom.2022.104336.

[22] U. Anwar, T. Arslan, and A. Hussain, "Hearing Loss, Cognitive Load and Dementia: An Overview of Interrelation, Detection and Monitoring Challenges with Wearable Non-invasive Microwave Sensors," Feb. 2022, doi: 10.1016/j.maturitas.2019.08.001.

[23] A. Hossain *et al.*, "Microwave brain imaging system to detect brain tumor using metamaterial loaded stacked antenna array," *Sci. Rep.*, vol. 12, no. 1, pp. 1–27, 2022, doi: 10.1038/s41598-022-20944-8.

[24] M. Cavagnaro, E. Pittella, and S. Pisa, "UWB pulse propagation into human tissues," *Phys. Med. Biol.*, vol. 58, no. 24, pp. 8689–8707, 2013, doi: 10.1088/0031-9155/58/24/8689.

[25] H. Zhang, A. O. El-Rayis, N. Haridas, N. H. Noordin, A. T. Erdogan, and T. Arslan, "A smart antenna array for brain cancer detection," *LAPC 2011 - 2011 Loughbrgh. Antennas Propag. Conf.*, vol. 2, no. November, pp. 1–4, 2011, doi: 10.1109/LAPC.2011.6114045.

[26] A. Arayeshnia, A. Keshtkar, and S. Amiri, "Realistic human head voxel model for brain microwave imaging," *2017 25th Iran. Conf. Electr. Eng. ICEE 2017*, pp. 1660–1663, 2017, doi: 10.1109/IranianCEE.2017.7985315.

[27] A. Ayd R. Saad, W. M. Hassan, and A. A. Ibrahim, "A monopole antenna with cotton fabric material for wearable applications," *Sci. Rep.*, vol. 13, no. 1, pp. 1–13, 2023, doi: 10.1038/s41598-023-34394-3.

[28] S. Wang, F. Kong, K. Li, and L. Du, "A planar triple-band monopole antenna loaded with an arc-shaped defected ground plane for WLAN/WiMAX applications," *Int. J. Microw. Wirel. Technol.*, vol. 13, no. 4, pp. 381–389, 2021, doi: 10.1017/S1759078720001099.

[29] A. S. M. Alqadami, K. S. Bialkowski, A. T. Mobashsher, and A. M. Abbosh, "Wearable Electromagnetic Head Imaging System Using Flexible Wideband Antenna Array Based on Polymer Technology for Brain Stroke Diagnosis," *IEEE Trans. Biomed. Circuits Syst.*, vol. 13, no. 1, pp. 124–134, 2019, doi: 10.1109/TBCAS.2018.2878057.

[30] E. Razzicchia, P. Lu, W. Guo, and P. Kosmas, "A New Metasurface-Enhanced Microstrip Patch Antenna for Haemorrhagic Stroke Detection," *15th Eur. Conf. Antennas Propagation, EuCAP 2021*, 2021, doi: 10.23919/EuCAP51087.2021.9410899.

[31] I. Saied, T. Arslan, S. Chandran, C. Smith, T. Spires-Jones, and S. Pal, "Non-Invasive RF Technique for Detecting Different Stages of Alzheimer's Disease and Imaging Beta-Amyloid Plaques and Tau Tangles in the Brain," *IEEE Trans. Med. Imaging*, vol. 39, no. 12, pp. 4060–4070, 2020, doi: 10.1109/TMI.2020.3011359.

[32] K. Furukawa *et al.*, "Increased Blood Viscosity in Ischemic Stroke Patients with Small Artery Occlusion Measured by an Electromagnetic Spinning Sphere Viscometer," *J. Stroke Cerebrovasc. Dis.*, vol. 25, no. 11, pp. 2762–2769, 2016, doi: 10.1016/j.jstrokecerebrovasdis.2016.07.031.

[33] G. Ziegelberger *et al.*, *Guidelines for limiting exposure to electromagnetic fields (100 kHz to 300 GHz)*, vol. 118, no. 5. 2020. doi: 10.1097/HP.0000000000001210.

[34] S. Candefjord *et al.*, "Microwave technology for detecting traumatic intracranial bleedings: tests on phantom of subdural hematoma and numerical simulations," *Med. Biol. Eng. Comput.*, vol. 55, no. 8, pp. 1177–1188, 2017, doi: 10.1007/s11517-016-1578-6.

[35] J. Kang *et al.*, "High blood viscosity in acute ischemic stroke," *Front. Neurol.*, vol. 14, no. November, pp. 1–7, 2023, doi:

10.3389/fneur.2023.1320773.
[36] I. M. Saied and T. Arslan, "Noninvasive Wearable RF Device Towards Monitoring Brain Atrophy and Lateral Ventricle Enlargement," *IEEE J. Electromagn. RF Microwaves Med. Biol.*, vol. 4, no. 1, pp. 61–68, 2020, doi: 10.1109/JERM.2019.2926163.
[37] S. Salahuddin, L. Farrugia, C. V. Sammut, M. O'Halloran, and E. Porter, "Dielectric properties of fresh human blood," *Proc. 2017 19th Int. Conf. Electromagn. Adv. Appl. ICEAA 2017*, no. October, pp. 356–359, 2017, doi: 10.1109/ICEAA.2017.8065249.
[38] D. B. Panagiotakos, "The Value of p-Value in Biomedical Research," *Open Cardiovasc. Med. J.*, vol. 2, no. 1, pp. 97–99, 2008, doi: 10.2174/1874192400802010097.
[39] "Guide to the expression of uncertainty in measurement," vol. 2024, no. Second Edition, 2024.
[40] W. F. Egan, *Practical RF System Design*. New Jersey: John Wiley & Sons, Inc., 2003. doi: 10.1002/0471654094.
[41] R. Ullah and T. Arslan, "Parallel delay multiply and sum algorithm for microwave medical imaging using spark big data framework," *Algorithms*, vol. 14, no. 5, 2021, doi: 10.3390/a14050157.

USMAN ANWAR received his B.S. in electrical (telecommunication) engineering from the National University of Computer and Emerging Sciences (NUCES), FAST, Islamabad, Pakistan in 2010 and his M.S. in telecommunication engineering from the University of Engineering and Technology, Taxila, Pakistan in 2016. He is currently pursuing his Ph.D. at the School of Engineering, The University of Edinburgh, Edinburgh, U.K. with a research focus on neurodegeneration detection through RF and microwave sensors.

His research interests include microwave and millimeter-wave antennas, Ultra-wideband MIMO and flexible biomedical sensors. He has an experience of over 10 years in the telecommunication industry; he worked as an Assistant Manager at Pakistan Telecommunication Company Limited from 2011 to 2016 and as Manager from 2016 to 2021 in the same organization.

TUGHRUL ARSLAN holds the Chair of Integrated Electronic Systems with the School of Engineering, The University of Edinburgh, Edinburgh, U.K. He is a member of the Integrated Micro and Nano Systems (IMNS) Institute and leads the Embedded Mobile and Wireless Sensor Systems (EWireless) Group with the University (ewireless.eng.ed.ac.uk). His research interests include developing low-power radio frequency sensors for wearable and portable biomedical applications. He is the author of more than 500 refereed papers and the inventor of more than 20 patents.

Prof. Arslan is currently an Associate Editor for the IEEE Transactions on VLSI Systems and was previously an Associate Editor for the IEEE Transactions on Circuits and Systems I (2005–2006) and IEEE Transactions on Circuits and Systems II (2008–2009). He is also a member of the IEEE CAS Executive Committee on VLSI Systems and Applications (1999 to date), and a member of the steering and technical committees of several international conferences. He is a co-founder of the NASA/ESA Conference on Adaptive Hardware and Systems (AHS) and currently serves as a member of its steering committee.

PETER LOMAX holds the position of Senior Experimental Officer at The University of Edinburgh, Edinburgh, U.K., managing the Scottish Microelectronics Centre within the School of Integrated Micro and Nano Systems (IMNS). Involved principally in research projects involving micro and nano fabrication technologies.

He has 24 years of industrial and academic experience, ranging from Radio Operator on an Antarctic research base to Principal Investigator (PI) on research projects. His research areas include X-ray emitter fabrication and MEMS/Nano detectors.

TOM RUSS is a Consultant Psychiatrist and Honorary Clinical Reader at the Centre for Clinical Brain Science, Division of Psychiatry at The University of Edinburgh, Edinburgh, U.K. He is the Director of the Alzheimer Scotland Dementia Research Centre. He trained in medicine and psychiatry in Edinburgh, the Highlands and London and works clinically with older people with functional mental illness and dementia. He is the secretary of the Royal College of Psychiatrists in Scotland philosophy and psychiatry special interest group and sits on the Working with Older People steering group at Human Development Scotland (formerly the Scottish Institute of Human Relations).